



Politecnico di Bari

Repository Istituzionale dei Prodotti della Ricerca del Politecnico di Bari

Modeling, Identification, and Control of a Dielectric Electro-Active Polymer Positioning System

This is a post print of the following article

Original Citation:

Modeling, Identification, and Control of a Dielectric Electro-Active Polymer Positioning System / Rizzello, G.; Naso, David; York, A.; Seelecke, S.. - In: IEEE TRANSACTIONS ON CONTROL SYSTEMS TECHNOLOGY. - ISSN 1063-6536. - 23:2(2015), pp. 632-643. [10.1109/TCST.2014.2338356]

Availability:

This version is available at <http://hdl.handle.net/11589/5995> since: 2022-06-27

Published version

DOI:10.1109/TCST.2014.2338356

Terms of use:

(Article begins on next page)

Modeling, Identification and Control of a Dielectric Electro-Active Polymer Positioning System

Gianluca Rizzello, David Naso, *Senior Member, IEEE*, Alexander York, Stefan Seelecke

Abstract: This paper deals with a positioning system based on a dielectric electro-active polymer membrane. The motion is generated by the deformation of the membrane caused by the electrostatic compressive force between two compliant electrodes applied on the surface of the polymer. The paper proposes a detailed electro-mechanical nonlinear model of the system, which is subsequently used to develop (in both time and frequency domains) various model-based feedback control laws. Accurate modeling is useful to compensate the nonlinear behavior of the actuator (caused by the material characteristics and geometry) and obtain PID controllers providing precise tracking of steps or sinusoidal reference signals. The various design strategies are compared on various experimental tests.

Index Terms- Smart Materials, Electro-Active Polymers, Precision Motion Control, PID, Mechatronics.

I. INTRODUCTION

SMART materials such as piezoelectric ceramics, magnetostrictives, thermal or magnetic shape memory alloys have shown to be an effective means to achieve increased accuracy and efficiency standards while reducing weights in many application fields, ranging from positioning systems to vibration dampers.

Electro-Active Polymers (EAPs) are a relatively newer class of smart materials reacting to electrical or chemical stimuli with a deformation that, in some cases, can be several orders of magnitude higher than that obtained with common materials such as piezoelectric ceramics. Dielectric EAP (DEAP) are a specific type of EAP in which controllable deformation is generated by an elastic polymeric material subject to compressive electrostatic forces between compliant electrodes applied on its surface. DEAP are attractive because of their lightweight, high energy density, fast response and low costs. Prototypes of DEAP pumps [1]–[4], valves [5], [6], speakers [7], [8], robots [9]–[11], lens element actuators [12]–[14] and micropositioning stages [15] have been documented in recent literature. On the other hand, there are many technological issues that still need to be properly addressed to make this material competitive in industrial applications,

such as the amount of voltage needed to obtain the deformation and the dependence of the response to temperature and fatigue. It has been remarked that the design of feedback control systems is a possible way to partly overcome these limitations, but to date most of the recent research efforts on DEAP still focus on material static and dynamic characterization [16]–[18], and on the accurate analysis of the underlying physical phenomena [19]–[26]. Among the few recent contributions exploring the role of feedback control in DEAP-based devices, it is useful to mention [27], which develops an embedded DEAP sensing and actuation system where the capacitance is calculated in real time and the resulting feedback is fed to a PID controller. Similarly, in [28], Randazzo et al. explored the controllability of a rotational joint driven by two DEAP arranged in an antagonistic configuration, and implemented a closed loop control for regulating both angular position and force. Sarban and Jones used a DEAP tubular actuator for realizing active vibration isolation by an internal model controller with gain-scheduling [29] and with an adaptive feedforward approach [30]. In [31], Wilson et al. compared the performance of a biomimetic, cerebellar-inspired controller with a conventional adaptive control scheme on a DEAP actuator, showing how the first strategy outperforms the second when the actuator characteristics change significantly.

This paper aims at contributing to this research direction, presenting a model of an innovative, miniaturized, precise positioning system based on an annular DEAP membrane, and analyzing the effects of various model-based control schemes. In particular, the model is more general, detailed and accurate with respect to those used in related literature, as it considers the particular geometry of the membrane to be taken into account and it directly incorporates the effects of the mass-spring preloading elements. Moreover, the model is used to develop a number of alternative model-based PID laws (including some nonlinear variants), which are implemented and compared on an experimental bench in a wide range of operative conditions. The resulting study contributes to better assess the actual potentialities and limitations of DEAP as an alternative technology for low cost positioning. This paper is also an extension of the preliminary ideas presented in the conference paper [32].

The reminder of this paper is organized as follows. Section II develops the model of the considered device, while Section III focuses on model validation and parameter identification. Section IV considers the control design problem, and formulates a number of alternative approaches in time and frequency domains. The experimental

The authors would like to acknowledge the support of Parker Hannifin, BioCare Business Unit.

G. Rizzello and D. Naso are with the Department of Electrical and Information Engineering, Politecnico di Bari, Bari, IT (e-mail: naso@deemail.poliba.it).

A. York and S. Seelecke are with the Department of Mechatronics, Universität des Saarlandes, Saarbrücken, DE (e-mail: alexander.york@mmsl.uni-saarland.de, stefan.seelecke@mmsl.uni-saarland.de).

comparison of the closed loop systems is provided in Section V, while Section VI provides the concluding remarks.

II. DEAP ACTUATOR MODEL

The device considered in this paper is based on the circular DEAP membrane shown in Fig. 1, while a sketch of the membrane in the undeformed resting condition and in the deformed condition is shown in Fig. 2 (a) and (b), respectively. The same membrane shape has also been considered in [17], although with partly different materials. The outer frame and the inner circular plate are made of rigid plastic (in green), while the 50 μm DEAP silicon membrane (in gray) is sandwiched between compliant electrodes. In particular, the membrane is pre-stretched during the production process, and once completed, the carbon grease electrodes are screen-printed all over the annular area of the polymeric film.

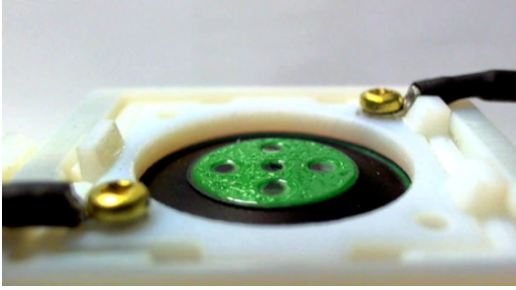


Fig. 1. The DEAP annular membrane.

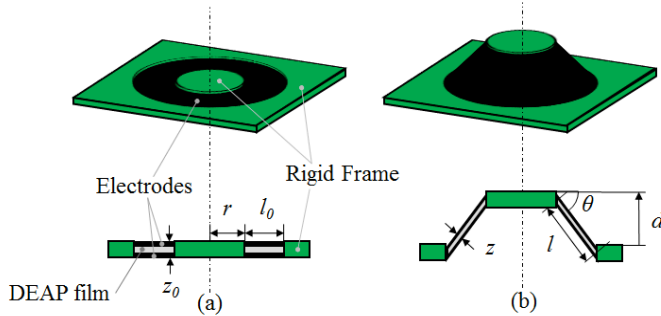


Fig. 2. DEAP membrane geometry in the undeformed (a) and deformed configuration (b).

A mass and a linear spring are connected to the moving part of the membrane, and constitute the actuator's load. The actuator out-of-plane stroke and actuation force can be tuned by choosing different loading elements, such as masses, linear and nonlinear springs (as discussed in [33]). When a voltage is applied to the electrodes, it generates a pressure known as Maxwell Stress [34] that compresses the material in the thickness direction, producing a radial expansion and the subsequent actuation motion shown in Fig. 3.

In the following section, we develop a dynamic model composed of a set of nonlinear, time-invariant differential equation describing the dynamic relationship between the input voltage and the output actuator displacement. The goal of the model is describing accurately the behavior of the device, both in transient and steady state performances, for various values of the load parameters in terms of mass and spring stiffness and pre-compression. The model extends the preliminary ideas presented in [24].

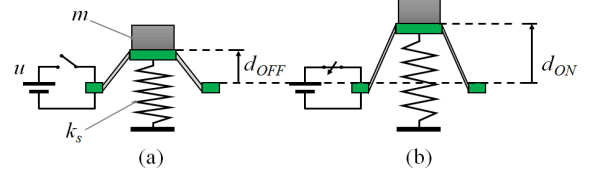


Fig. 3. Actuation mechanism, input voltage off (a) and on (b).

A. Mechanical dynamics

The model considers the voltage applied to the membrane u as input and the vertical displacement d as output (Fig. 3). The vertical force equilibrium on the biasing mass can be expressed as follows

$$m(\ddot{d} + g) + k_s(d - d_s) + \eta_s \dot{d} + F_{DEAP}(u, d, t) \sin \theta = 0, \quad (1)$$

where m is the mass of the load (the mass of the central rigid plate is neglected), g is the gravitational acceleration, F_{DEAP} is the polymer reaction force, t is time, θ is the deflection angle of the membrane, k_s is the load spring stiffness and d_s represents the spring pre-compression. To consider the non-ideal behavior of the spring, we introduce a further contribution η_s modeling a small viscous damping phenomenon.

To take into account the particular shape of the polymeric membrane, it can be observed that the DEAP reaction force acting on the inner plastic plate is given by the product of the radial stress of the material, hereafter indicated with $\sigma_r(d, u, t)$, times the cross-sectional area. Therefore, it holds

$$F_{DEAP}(d, u, t) = 2\pi r z \sigma_r(d, u, t), \quad (2)$$

where z is the actual material thickness and r is the radius of the inner rigid frame. The dependence of F_{DEAP} and σ_r from time t in (2) is introduced to indicate that the link with the variable d and u is dynamic. Since the Poisson ratio of the silicone is 0.5, it is realistic to assume that the DEAP material volume remains constant during excitation, and the relation between variables z and d can be easily obtained by simple geometrical considerations. In particular, it can be shown (see [24] for further details) that

$$z = z_0 \frac{l_0}{l} = z_0 \frac{l_0}{\sqrt{l_0^2 + d^2}}, \quad (3)$$

where z_0 and l_0 are the initial values of the thickness z and radial length l indicated in Fig. 2. Substituting (3) into (2), and rewriting the sine as the ratio of d and l , the force generated by the DEAP can be rewritten as follows:

$$F_{DEAP}(d, u, t) \sin \theta = 2\pi r z_0 l_0 \frac{d}{l_0^2 + d^2} \sigma_r(d, u, t). \quad (4)$$

B. Material behavior model

The model of the smart material analyzes the dependency of the radial stress in (4) to the applied voltage. Clearly, the model can be extended to other types of membranes by adapting (4) to the specific geometry of the DEAP. Here it is assumed that the electrodes mechanics can be neglected due

to their small thickness in comparison to the thickness of the silicon. The development of this part of the model is based on the free-energy approach proposed by Suo et al. [35]. The approach determines the relationships between electrical and mechanical variables with a reasoning based on free-energy functions. More specifically, this part of the model is obtained in two steps. First the energy approach is used to determine the static relations between electrical and mechanical quantities, and then the equations are modified to take into account the dynamics introduced by material viscoelasticity.

For the circular geometry, the state of deformation of the membrane is described by the radial, circumferential and thickness stretches, denoted as λ_r , λ_c , and λ_z , respectively [36]. A pre-stretch also exist into the DEAP membrane because of its manufacturing process, and to take it into account, the following quantities are defined [37]:

$$\lambda_{r,tot} = \lambda_r \lambda_{r,pre}, \quad (5)$$

$$\lambda_{c,tot} = \lambda_c \lambda_{c,pre}, \quad (6)$$

$$\lambda_{z,tot} = \lambda_z \lambda_{z,pre}. \quad (7)$$

The symbol $\lambda_{i,tot}$ represents the total stretch in the i -th principal direction, and is equal to the product of the actuation stretch λ_i and the (constant) pre-stretch $\lambda_{i,pre}$. Since the material is incompressible in each state of deformation, the following equality holds

$$\lambda_{r,tot} \lambda_{c,tot} \lambda_{z,tot} = \lambda_r \lambda_c \lambda_z = \lambda_{r,pre} \lambda_{c,pre} \lambda_{z,pre} = 1. \quad (8)$$

By assuming that the membrane deformation follows a truncated-cone geometry (as depicted in Fig. 2), the circumferential actuation stretch is constant and equal to 1 (the same cannot be stated a priori for the circumferential pre-stretch, due to the lack of detailed information on the manufacturing process of the membrane). Due to this assumption, it holds

$$\lambda_r = \frac{l}{l_0} = \frac{\sqrt{l_0^2 + d^2}}{l_0}, \quad (9)$$

$$\lambda_c = 1, \quad (10)$$

$$\lambda_z = \frac{z}{z_0}. \quad (11)$$

It can be noted that the product of the three quantities above, in conjunction with the effects of incompressibility stated by (8), confirms the result given in (3). The free-energy density function W can be obtained as the sum of deformation and electric charge energies. Thus,

$$W = \sum_{i=1}^N \frac{\mu_i}{\alpha_i} \left(\lambda_{r,tot}^{\alpha_i} + \lambda_{c,tot}^{\alpha_i} + \lambda_{z,tot}^{\alpha_i} - 3 \right) + \frac{D^2}{2\epsilon_0 \epsilon_r}, \quad (12)$$

where the first contribution represents the deformation energy by means of an Ogden hyperelastic model [37], μ_i and α_i are material constitutive parameters and N is the number of terms in the Ogden energy function. The quantity D appearing in the second energetic term is the electrical displacement, namely the charge density over the electrodes

surfaces assuming an ideal behavior of the DEAP, ϵ_0 is vacuum permittivity and ϵ_r is the relative permittivity of the polymeric material. The thickness stretch in (12) can be eliminated due to the incompressibility assumption (8) as suggested in [35], i.e.,

$$W = \sum_{i=1}^N \frac{\mu_i}{\alpha_i} \left(\lambda_{r,tot}^{\alpha_i} + \lambda_{c,tot}^{\alpha_i} + \lambda_{r,tot}^{-\alpha_i} \lambda_{c,tot}^{-\alpha_i} - 3 \right) + \frac{D^2}{2\epsilon_0 \epsilon_r}. \quad (13)$$

Then, the actual radial stress σ_r and the actual electric field E can be obtained by differentiating the (13) as follows:

$$\sigma_r = \lambda_{r,tot} \frac{\partial W(\lambda_{r,tot}, \lambda_{c,tot}, D)}{\partial \lambda_{r,tot}} - ED, \quad (14)$$

$$E = \frac{\partial W(\lambda_{r,tot}, \lambda_{c,tot}, D)}{\partial D}. \quad (15)$$

After differentiation, one obtains

$$\sigma_r = \sum_{i=1}^N \left(\beta_i \lambda_r^{\alpha_i} - \gamma_i \lambda_r^{-\alpha_i} \right) - \epsilon_0 \epsilon_r E^2, \quad (16)$$

where

$$\beta_i = \mu_i \lambda_{r,pre}^{\alpha_i}, \quad (17)$$

$$\gamma_i = \mu_i \lambda_{z,pre}^{\alpha_i}. \quad (18)$$

Finally, substituting the electrical field E with the ratio of voltage and thickness, i.e.,

$$E = \frac{u}{z} = \frac{u}{z_0 \lambda_z} = \frac{u \lambda_r}{z_0}, \quad (19)$$

the (16) can be rewritten as

$$\sigma_r = \sum_{i=1}^N \left(\beta_i \lambda_r^{\alpha_i} - \gamma_i \lambda_r^{-\alpha_i} \right) - \epsilon_0 \epsilon_r \left(\frac{u \lambda_r}{z_0} \right)^2. \quad (20)$$

According to (20), the radial stress depends directly only on the actuation radial stretch λ_r and on the square of the applied voltage u . The effects of pre-stretches are lumped into coefficients β_i and γ_i (see eq. (17)-(18)), and results in a non-zero stress appearing when no voltage is applied ($u = 0$) and the membrane is in its undeformed state ($\lambda_r = 1$). Equation (20) well describes the hyperelasticity and the electro-mechanical coupling effects of DEAP, but it does not take into account material viscoelasticity. This motivates the next step of the material modeling procedure.

A possible way to take into account the effects of viscoelasticity is interpreting (20) by considering the total radial stress equal to the sum of two terms: an elastic contribution σ_e due to the stretch and a Maxwell stress σ_m due to the electromechanical coupling. Thus,

$$\sigma_r = \sigma_m + \sigma_e. \quad (21)$$

In (21), σ_m is the Maxwell stress and is given by

$$\sigma_m = -\varepsilon_0 \varepsilon_r \left(\frac{u \lambda_r}{z_0} \right)^2, \quad (22)$$

while the σ_e term is modeled as a dynamic viscoelastic process. The effects of viscoelasticity can be effectively described by spring-dashpot rheological model [39]. In particular, the nonlinear model in Fig. 4 (the nonlinearity consists only in the parallel spring labeled as “Ogden spring”) is used to describe the dynamics of σ_e .

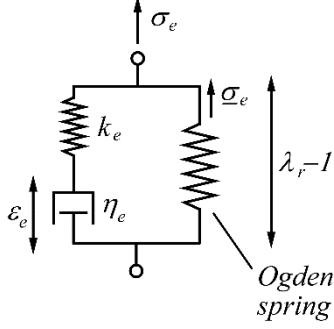


Fig. 4. The viscoelastic model, a nonlinear version of a standard linear solid model.

The complete the viscoelastic model is then provided by

$$\begin{cases} \dot{\varepsilon}_e = -\frac{k_e}{\eta_e} \varepsilon_e + \frac{k_e}{\eta_e} (\lambda_r - 1) \\ \sigma_e = -k_e \varepsilon_e + k_e (\lambda_r - 1) + \underline{\sigma}_e \end{cases}, \quad (23)$$

where $\underline{\sigma}_e$ is the steady state value of σ_e under constant voltage excitation $u \equiv \underline{u}$, which can be computed as follows

$$\underline{\sigma}_e = \sum_{i=1}^N \left(\beta_i \lambda_r^{\alpha_i} - \gamma_i \lambda_r^{-\alpha_i} \right), \quad (24)$$

where the underlined variable indicate the constant value under static conditions. Equations (21)-(24) equation reference goes here are coherent with (20) at steady state, and also describe the dynamics of the viscoelastic process during the transient response.

C. Complete actuator model

For control design purposes, equations

Errore. L'origine riferimento non è stata trovata. (4), (21)-(24) can be merged so as to obtain the complete third-order, nonlinear, time-invariant, state-space model shown in equation (27) at the bottom of the page. Model state vector $x(t)$ is defined as

$$x(t) = \begin{bmatrix} \varepsilon_e(t) & d(t) & \dot{d}(t) \end{bmatrix}^T, \quad (25)$$

while the nonlinear function $s(x_2)$, introduced to obtain a more compact notation, is defined as

$$s(x_2) = 1 + \frac{x_2^2}{l_0^2}. \quad (26)$$

The parameters a_{ij} are summarized in Table I. The identification of the unknown values of these parameters is discussed in the next section.

TABLE I
DEAP MODEL COEFFICIENTS

Parameter	Explicit equation
a_{11}	k_e/η_e
a_{21}	$k_s d_s/m - g$
a_{22}	k_s/m
a_{23}	η_s/m
a_{24}	$2\pi r z_0/m l_0$
a_{25}	k_e
a_{26}	$\varepsilon_0 \varepsilon_r / z_0^2$

III. PARAMETER IDENTIFICATION AND MODEL VALIDATION

The effectiveness of the model developed in the previous section is assessed on the experimental platform shown in Fig. 5, consisting of DEAP membrane, mass and spring load (experiments are carried out with three different load springs, whose stiffness and damping coefficients are indicated hereafter as k_{s1} , k_{s2} , k_{s3} and η_{s1} , η_{s2} , η_{s3} respectively), a TREK 610E voltage amplifier (max applicable voltage = 10 kV, max current = 2 mA), a Keyence LK-G37 laser displacement sensor (0.15 μ m resolution), A Futek LSB-200 load cell (1 μ N resolution)

$$\begin{cases} \dot{x}_1 = -a_{11} \left[x_1 - \sqrt{s(x_2)} + 1 \right] \\ \dot{x}_2 = x_3 \\ \dot{x}_3 = a_{21} - a_{22}x_2 - a_{23}x_3 - a_{24} \frac{x_2}{s(x_2)} \left\{ \sum_{i=1}^3 \left(\beta_i s(x_2)^{\frac{\alpha_i}{2}} - \gamma_i s(x_2)^{-\frac{\alpha_i}{2}} \right) \right\} - a_{25} \left[x_1 - \sqrt{s(x_2)} + 1 \right] - a_{26} s(x_2) u^2 \\ y = x_2 \end{cases} \quad (27)$$

controlled with a linear actuator (Aerotech, model ANT-25LA) and a Zaber LA-28A linear actuator connected to the load spring to modify the pre-compression and apply load disturbances.

The known or measurable parameters of the DEAP testing bench are summarized in Table II. The remaining parameters of the model, namely the Ogden model order N and coefficients α_i , β_i and γ_i for $i=1, \dots, N$, the coefficients of the viscoelastic model k_e and η_e , the springs damping coefficients η_s , and the relative permittivity ϵ_r must be identified with appropriated methods. When recording the system dynamics with a computer-based DAQ system, a first order low-pass filter (with a time constant equal to 6.4ms) is included in cascade with the DEAP actuator model in each simulation to model the behavior of the data acquisition hardware.

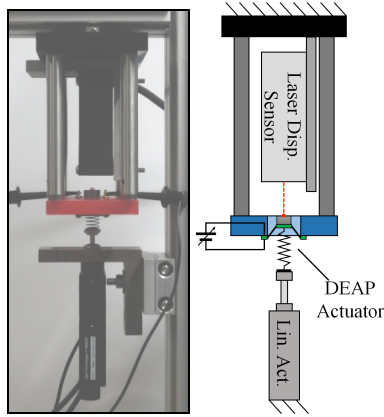


Fig. 5. The DEAP actuator system, picture (left) and sketch (right).

TABLE II
KNOWN ACTUATOR SYSTEM COEFFICIENTS

Coefficient	Value	Unit
z_0	40	μm
l_0	4.75	mm
r	6.25	mm
ϵ_0	$8.85 \cdot 10^{-12}$	F/m
g	9.81	m/s^2
m	7.10	g
k_{s1}	0.05	N/mm
k_{s2}	0.22	N/mm
k_{s3}	0.34	N/mm

Only a subset of the unknown parameters, i.e., ϵ_r , α_i , β_i and γ_i , influences the quasi static behavior of the material and therefore is identified first with a set of *ad hoc* experiments in which the load spring is removed and the linear motor is directly connected to the DEAP membrane, to change the position while no voltage is applied to the electrodes. The linear motor applies a very slow (5 mHz) sinusoidal motion for static characterization (other tests with slower signals led to the same results). Once force and displacement measurements are available, stress and strain are reconstructed by means of the model equations. In this paper, to limit the complexity of the identification algorithm, the Ogden model order and exponents are selected a priori, basing on preliminary information. In particular, we set $N = 3$ and coefficients α_i equal to the three lowest even integers to replicate the expected convex

behavior of the modeled functions. The remaining unknown coefficients ϵ_r , β_i and γ_i are identified by using a standard least square algorithm [40]. The results of this identification are summarized in Fig. 6. The overlap between the experimental and model behaviors is satisfactory. A small hysteresis introduced by the mechanical behavior of the compliant electrodes is observed (also in tests with slower signals) between the two variables, but the resulting error seems sufficiently minor to avoid the introduction of further components in the model. The coefficients values of this identification stage are reported in Table III.

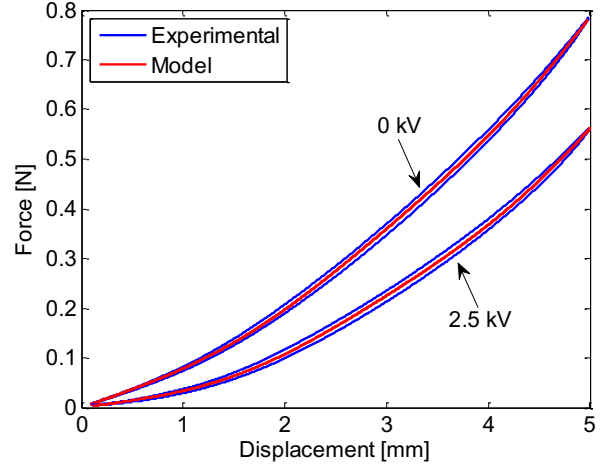


Fig. 6. Static model identification, experimental (blue) and model (red).

The remaining model parameters appearing in the force equilibrium equation **Error. L'origine riferimento non è stata trovata.** and in the viscoelastic model (23) only affect the transient behavior, and therefore they are identified by means of nonlinear optimization techniques. In particular, while the viscoelastic model coefficients characterize material inherent damping, the coefficients η_{s1} , η_{s2} and η_{s3} describe the different damping contributions introduced by each spring, and are identified separately. First an Amplitude Modulated Pseudo Random Binary Signal (APRBS) input signal with a maximum switching frequency of 30 Hz, amplitude in the range 0 – 2.5 kV and a duration of 60 s is applied when the actuator is pre-loaded with the spring k_{s2} and pre-stretched in order to obtain a membrane static pre-deflection of 2 mm. This permits to identify the viscoelastic model coefficients and the spring damping η_{s2} . Then, the remaining spring damping coefficients η_{s1} and η_{s3} are determined, in conjunction with the previously identified material viscoelastic coefficients, by matching the system response to a square wave input signal. Several iterations of these two steps allow to characterize each unknown coefficient. Fig. 7 shows the system response and the resulting best-fit model. Also the results of this part of the identification procedure are satisfactory, as the model reproduces fairly well the underdamped dominant behavior visible in Fig. 7 for the APRBS training signal.

Validation is performed with a biased sine sweep of linearly increasing frequency up to 50 Hz and amplitude ranging from 0 to 1.5 kV, and the results are shown in the frequency domain. In particular, **Error. L'origine riferimento non è stata trovata.** Fig. 8 shows results for several validation tests, performed for three different springs (see Table II) and three different membrane pre-deflections

for each spring. It can be noticed how the model shows a good ability to predict the natural frequency as it varies from 20 to 45 Hz, under different biasing conditions.

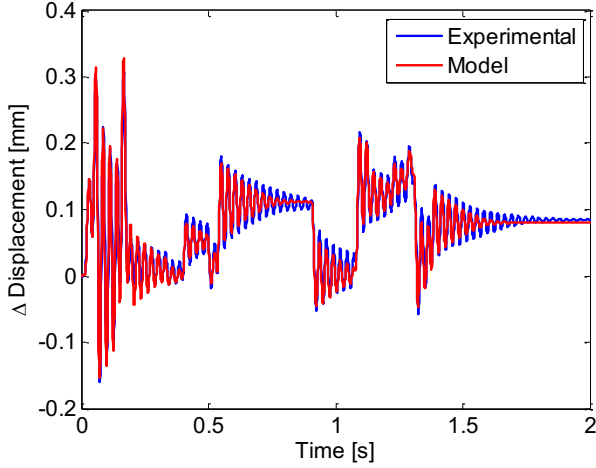


Fig. 7. APRBS identification test, experimental (blue) and model (red) output displacement.

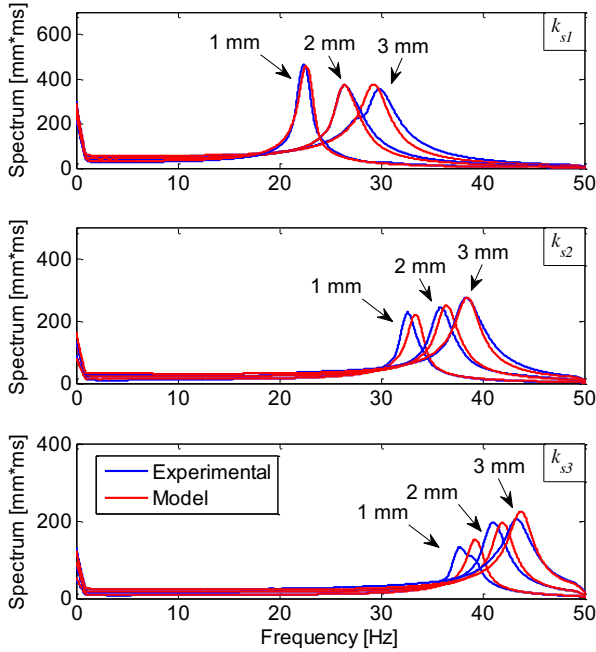


Fig. 8. Sine sweep (from 0 to 1.5 kV) response spectrum for different springs and DEAP pre-deflections, experimental (blue) and model (red).

TABLE III
IDENTIFIED MODEL PARAMETERS

Coefficient	Value	Unit
α_1	2	-
α_2	4	-
α_3	6	-
β_1	-7.05	MPa
β_2	3.72	MPa
β_3	-0.54	MPa
γ_1	-17.58	MPa
γ_2	21.06	MPa
γ_3	-7.57	MPa
ϵ_r	3.92	-
k_e	0.48	MPa
η_e	4.37	kPa·s
η_{s1}	$6.48 \cdot 10^{-6}$	N·s/mm

η_{s2}	$21.86 \cdot 10^{-6}$	N·s/mm
η_{s3}	$30.48 \cdot 10^{-6}$	N·s/mm

IV. CONTROLLERS DESIGN

The main control design objective for the considered prototype is to obtain a fast and accurate tracking of steps signals of various amplitude. Saturation of control action for long time intervals and chattering must be avoided to prevent excessive stress to the hardware. In particular, the applied voltage cannot exceed the range 0 - 2.5 kV. The selected closed loop reference model has second order underdamped dynamics with damping factor $\delta = 0.8$ (a typical design choice to avoid resonating behaviors) and a variable natural frequency ω_n used to tune the closed loop time constant τ_{cl} . The design is performed in continuous time, and the implementation is carried out in the digital domain with trapezoid rule and sampling time of 1 ms, and anti-windup algorithms. In order to reduce the high-frequency effects introduced by the derivative action, all the PID controllers described in the next sections are cascaded with a linear first order filter whose time constant τ_f is considered as a further design parameter [41]. The controller transfer function has therefore the following form:

$$G_{PID}(s) = \frac{1}{\tau_f s + 1} \left(k_p + \frac{k_i}{s} + k_d s \right) \quad (28)$$

Design criteria for the considered controllers are discussed in the next subsections, and the final parameters of the resulting controllers are summarized in Table IV at the end of the section.

A. Standard PID design

The first controller is a standard linear PID. The design is based on a linear model of the DEAP actuator obtained by linearization of the model (27) around a predefined equilibrium point corresponding to a constant input \underline{u} . After linearization, the first order dynamics introduced by the laser displacement sensor (as discussed in Section III) is added to the open loop plant transfer function. Independently of the chosen equilibrium point, it can be easily proven that the linearized model is characterized by two dominant complex poles, two stable real poles and one minimum phase zero. Since the zero is always located very close to one of the real poles, their mutual cancellation reduces the order of the model without causing significant losses of model accuracy or closed-loop performance. Fig. 9 shows the Bode diagram for three different voltage levels \underline{u} , corresponding to the minimum, intermediate and maximum applicable voltage. It can be noted that the static gain of the linearized model decreases for decreasing values of the equilibrium voltage, until the linearized model degenerates in an uncontrollable model for $\underline{u} = 0$.

The free parameters of the PID controller are chosen so that the two zeros of the controller cancel the complex poles of the linearized model, and the residual dynamics leads to a closed loop function with the predefined damping and natural frequency, which is chosen in order to achieve the closed loop time constant $\tau_{cl} = 56$ ms.

This control will be hereafter referred to as *PID/TD* (PID designed in Time Domain). For all the controllers, the value of the voltage at which the linearization is performed will be indicated in brackets.

B. Nonlinear PID design

Among the various causes of nonlinearity in the DEAP actuator, the analysis of (27) reveals that both static and dynamic behaviors of the displacement are influenced by the square of the voltage. A straightforward approach to limit the effects of this nonlinearity is to cancel it by inverse compensation in controller output law. This is obtained with the scheme in Fig. 10, in which the controller output is computed as the square root of the output of the linear PID, i.e.

$$u = f(w) = w^{1/2}. \quad (29)$$

The design of the PID law in this case is obtained by considering $f(w)$ as part of the controlled plant, performing linearization of the dynamics between w and y , and using the same criteria described in the previous subsection to choose the controller gains.

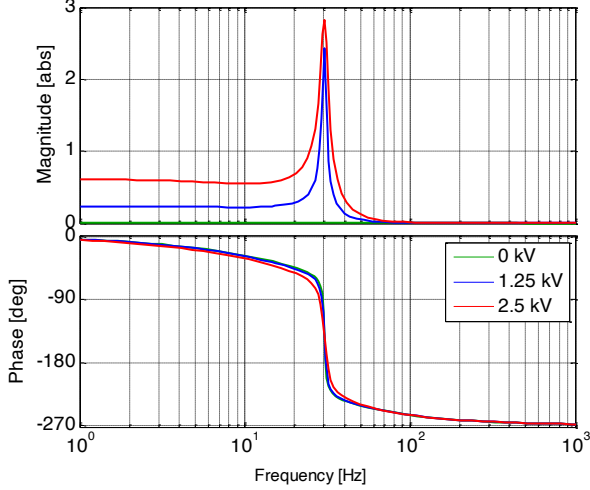


Fig. 9. Linearized model Bode diagram, different voltages (note the linear scale for the Amplitude diagram). The resonances are caused by a couple of complex poles having the following damping coefficients: $\delta = 0.028$ (1.25 kV), $\delta = 0.055$ (2.5 kV).

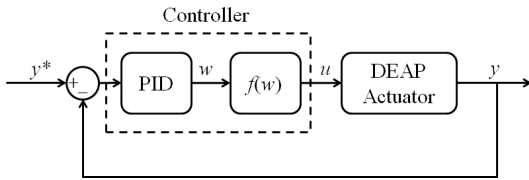


Fig. 10. PID plus nonlinear compensation block diagram.

The Bode diagram of the new linearized model, evaluated for different input voltages, is shown in Fig. 11. The static nonlinearity cancellation leads to a strong reduction of the differences between the models at various operating points. Note that, differently from Fig. 9, to better analyze the effects of nonlinearity cancellation, we include the further model obtained by linearization around the intermediate constant input voltage equal to 1.77 kV. To isolate the effects of nonlinearity cancellation, the PID is tuned using

the same design criterion adopted for the previously described controller (closed loop time constant $\tau_{cl} = 56$ ms). This controller will be referred to as *NPID/TD* (Nonlinear PID design in time domain). A second version of this controller is also considered in the comparison. More specifically, by hand-tuning, it has been observed that the best tradeoff in terms of closed loop response time, oscillations, and saturation avoidance can be obtained by imposing a closed loop time constant $\tau_{cl} = 23$ ms. This second version of the controller will be referred to as *NPID/TDO* (Nonlinear PID design in Time Domain with Optimized tuning).

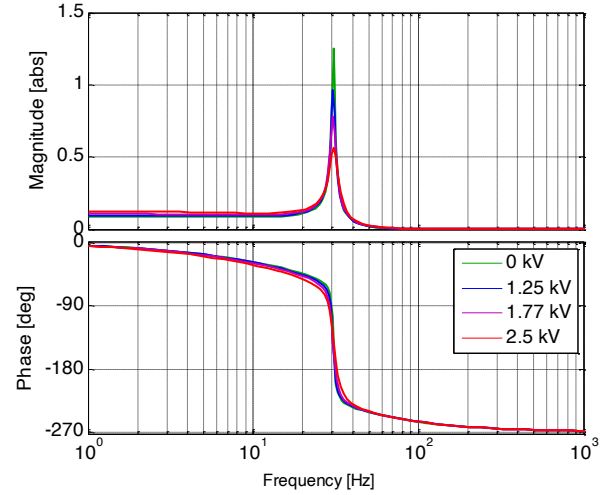


Fig. 11. Compensated linearized model Bode diagram, different voltages. The resonances are caused by a couple of complex poles having the following damping coefficients: $\delta = 0.020$ (0 kV), $\delta = 0.028$ (1.25 kV), $\delta = 0.036$ (1.77 kV), $\delta = 0.055$ (2.5 kV).

C. Nonlinear robust PID design

The compensation by inverse cancellation of input nonlinearity contributes to mitigate its effects on the closed loop performance in a wide range of operating point, but it does not provide specific guarantees about the performance degradation caused by the remaining nonlinearities. A possible way to overcome this limitation is describing the controlled system as a family of linear models, obtained by linearization at various equilibrium points, and using robust control tools to perform the controller design. The method will be applied in conjunction with the static nonlinearity cancellation described in the previous subsection. In particular, in this section we use the standard direct loop-shaping H_∞ robust control design approach (see [42] for a comprehensive introduction). The system is described with the following multiplicative uncertainty

$$G(s) = [1 + \Delta(s)w_i(s)]G_n(s), \quad (30)$$

where $G_n(s)$ is the nominal transfer function (obtained by linearization around $\underline{u} = 1.77$ kV), $w_i(s)$ is a shaping transfer function and $\Delta(s)$ is a random perturbation transfer function such that $\|\Delta(s)\|_\infty < 1$. As $\Delta(s)$ varies, $G(s)$ describes the whole linearized model set. Fig. 12 shows a shaping function $w_i(s)$ which includes all the linearized models in the considered voltage range. In order to take into account on unmodeled high frequency uncertainties, the system

robustness is tested with an upper bound of the actual $w_i(s)$ (in red in Fig. 12).

The design approach consists of properly choosing loop-shaping filters for closed-loop sensitivity and complementary sensitivity in order to guarantee the desired closed-loop properties under given model uncertainty, and then solving the design problem with numerical methods [42]. A condition based on the μ -norm upper bound is used to establish robust stability and performance of the uncertainty set independently on how fast the function $G(s)$ is perturbed [43]. After preliminary reasoning based on standard robust design criteria, the two sensitivity functions shown in Fig. 13 are selected as final filters. The H_∞ controller is numerically tuned imposing a low-sensitivity bandwidth greater than 3.25 Hz and no resonance peaks in the complementary sensitivity. The resulting H_∞ controller has a frequency response that is shown in Fig. 14. **Errore. L'origine riferimento non è stata trovata.**, together with a reduced order approximation of the controller at low frequencies, performed with a PID with low-pass filtered derivative action. The closed loop transfer functions obtained with the reduced order controller are also shown in Fig. 13. The reduced order controller will be referred to as $NPID/H_\infty D$ (Nonlinear PID with H_∞ design).

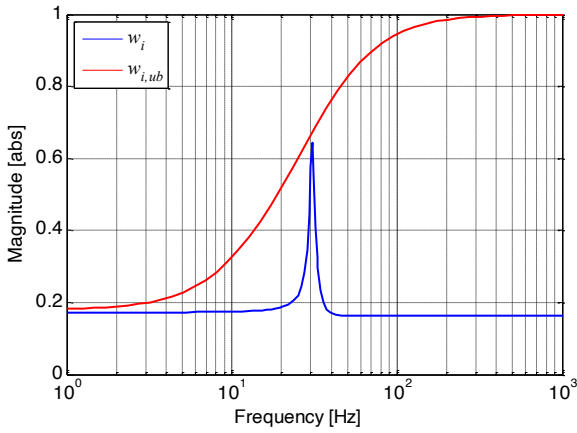


Fig. 12. Uncertainty set shaping function (blue) and upper bound (red).

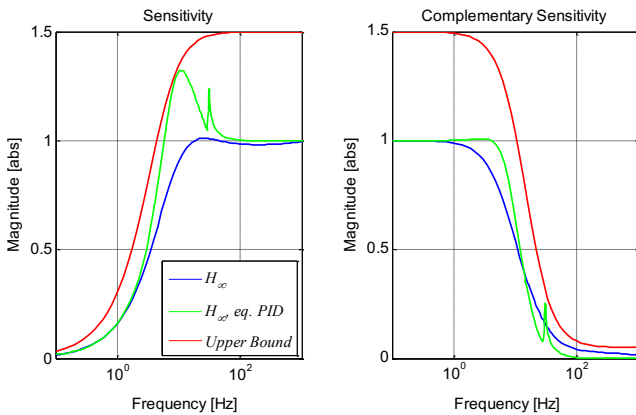


Fig. 13. H_∞ Sensitivity (left) and Complementary Sensitivity (right) Bode diagrams, comparison between original controller (blue) and PID approximation (green).

D. Sinusoidal tracking with resonant PI control

In addition to the previous controllers which are mainly designed for position regulation, and basing on internal

model design criteria, a controller suitable to track harmonic references is considered in this subsection for applications of the DEAP membrane in pumps or other vibrating devices. In order to improve the tracking performance without increasing controller complexity, the following PI-Resonant (PIR) controller is proposed (still applying the nonlinearity compensation of the previous subsection):

$$G_{PIR}(s) = k_p + \frac{k_i}{s} + \frac{k_r s}{s^2 + \omega_r^2}. \quad (31)$$

Differently from the PID in (28), the first order filter is unnecessary for this controller. If ω_r in (31) is set equal to the target frequency, this controller ensures perfect tracking at steady state for a linear plant. If the reference signal is a biased sinewave, the integral term permits also the tracking of the continuous component. The controller is tuned with an optimization algorithm that minimizes the L_2 norm of the tracking error for the desired reference profile. The controller will be referred to as $NPIR$ (Nonlinear PI + Resonant design).

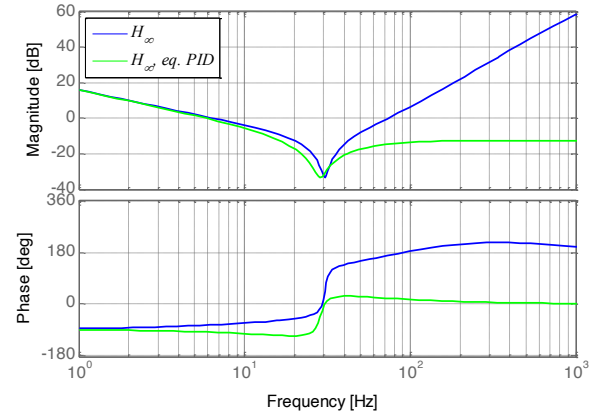


Fig. 14. H_∞ controller Bode diagram, original controller (blue) and low-frequency PID approximation (green).

TABLE IV
CONTROLLERS COEFFICIENTS

PID Controller	k_p	k_i	k_d	τ_f
<i>PID/TD</i> (1.25 kV)	0.017	60.54	0.002	0.02
<i>PID/TD</i> (2.5 kV)	0.013	23.63	0.001	0.02
<i>NPID/TD</i> (0 kV)	0.034	165.05	0.005	0.02
<i>NPID/TD</i> (1.25 kV)	0.044	151.35	0.004	0.02
<i>NPID/TD</i> (1.77 kV)	0.052	138.78	0.004	0.02
<i>NPID/TD</i> (2.5 kV)	0.067	118.15	0.003	0.02
<i>NPID/TDO</i> (1.77 kV)	0.121	321.69	0.009	0.005
<i>NPID/H_∞D</i> (1.77 kV)	0.266	366.29	0.011	0.005
PIR Controller	k_p	k_i	k_r	ω_r
<i>PIR</i> (5 Hz, 1.77 kV)	-5.810	53.39	66.34	$5 \cdot 2\pi$
<i>PIR</i> (15 Hz, 1.77 kV)	-0.8674	211.47	195.98	$15 \cdot 2\pi$

V. SIMULATION AND EXPERIMENTAL RESULTS

This section summarizes the experimental results of the controllers described in the previous section. Each plot compares experimental results (blue) and simulation (red) results in terms of actuator displacement (upper, the dashed

line represents the set-point), tracking error and input voltage (the black line represent the voltage bounds). The experimental setup is the same used for model identification and shown in Fig. 5. The results of the PID/TD is shown in Fig. 15, for $\underline{u} = 1.25$ kV. The response of this controller is satisfactory if the system operates in the neighborhoods of the equilibrium point, and it becomes excessively under or overdamped in other regions due to system nonlinearities. Similar results are obtained by tuning the controller on different equilibrium points. The figure also compares the simulated and experimental closed loop performances, showing a good agreement between the signals. Fig. 16 shows the performance of the $NPID/TDO$ controller. The effect of this compensation on the control performance are evident.

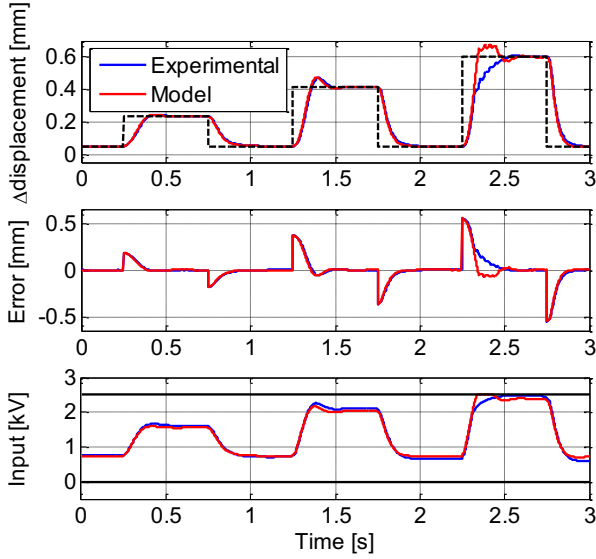


Fig. 15. PID/TD , tuned on the linearized model at 1.25 kV.

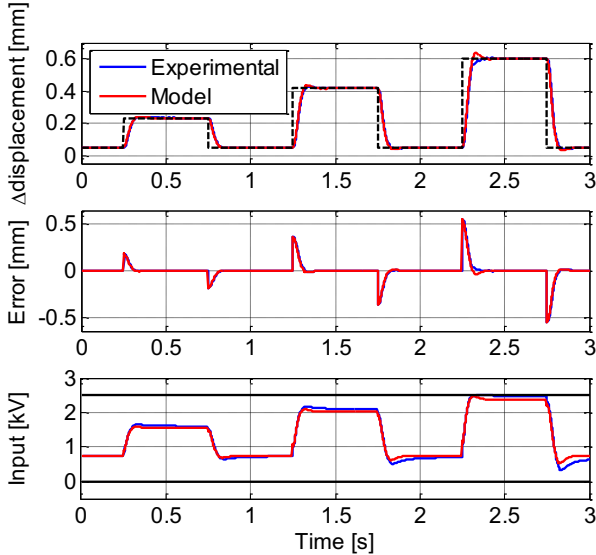


Fig. 16. $NPID/TDO$, with nonlinearity compensation, tuned on the linearized model at 1.77 kV, optimized tuning.

The response of the optimized PID is also very close to the PID tuned with the H_∞ design, shown in Fig. 17. In the tracking error plot in Fig. 17, a curve labeled as “bound” is also drawn, which corresponds to the response of the performance matrix producing an upper bound of μ -norm smaller than 1 (robust performance condition). The tracking error converges to zero always faster than this signal. A

comparison of tracking errors for the best controllers of each type is reported in Fig. 18, while experimental results for a disturbance rejection test for $NPID/TDO$ and $NPID/H_\infty D$ are shown in Fig. 19. The linear actuator is moved at constant velocity to a desired final position (see Fig. 5), changing the biasing spring pre-compression d_s in order to simulate a load disturbance, which is efficiently compensated by the control system. Finally, the performance of the $NPIR$ control for a 15 Hz reference is shown in Fig. 20. When a sine sweep reference is applied, the tracking error reaches its minimum when the input is at the resonance frequency ω_r , proving the effectiveness of this type of controller. The steady-state error peak is 14.89 μm . Table V summarizes the performance comparison using the L_2 norm of the tracking error ($\|e\|_2$), the average steady state error ($mean(e_{ss})$) and the average steady state error during control input saturation ($mean(e_{ss,sat})$). The quantity in brackets represents the equilibrium voltage of the linearized plant used for the design. The $NPID/H_\infty D$ shows the best performance in terms of all the proposed indices. $NPID/TDO$ on the other hand performs very close to $NPID/H_\infty D$, which is much more demanding in terms of manual and numerical design effort. In order to reduce the emphasis on the transient error occurring during reference step changes, Table VI shows the results of the same controllers while tracking a low-pass filtered step reference. The chosen reference filter is a second order linear filter with unitary gain and a double pole $p_f = -50$. In this further test, the error peak ($\|e\|_\infty$) is also considered in the comparison. The faster controllers, namely $NPID/TDO$ and $NPID/H_\infty D$, exhibit the smaller error peaks (275 and 260 μm respectively), while the other controllers exhibit significantly worse performance.

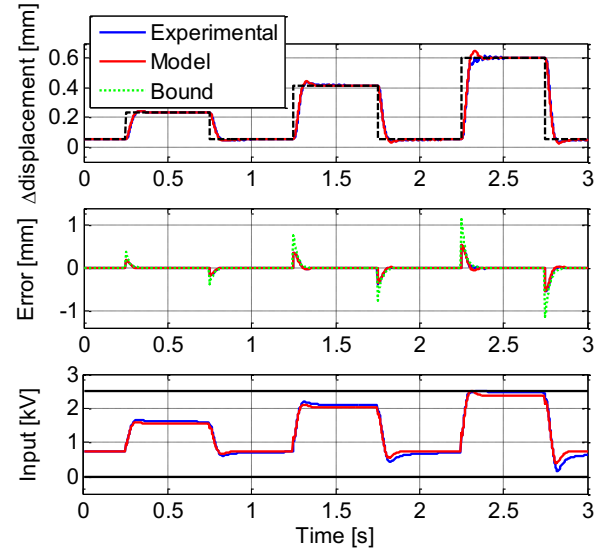


Fig. 17. $NPID/H_\infty D$, with nonlinearity compensation, tuned on the linearized model at 1.77 kV.

VI. CONCLUSIONS

This paper has developed a model of a positioning system based on a DEAP annular membrane, and proposed a number of model-based feedback controllers. The experimental comparison suggests that a simple cancellation of the nonlinearity on the main input of the system (the applied voltage) contributes to significantly improve the performances of controllers designed by means of

linearization, reaching in many cases the maximum level of precision allowed by the considered sensor. This approach can be combined with other robust control design tools, such as H_∞ design, to obtain extremely accurate tracking performance along with a quantitative characterization of the effects of the residual uncertainties in the model. The case of sinusoidal reference tracking has also been satisfactorily addressed with another variant of the PID including a resonant term. In conclusion, the development of appropriately tuned linear strategies permits to obtain satisfactory performances on the particular type of DEAP actuator considered in this paper.

The paper leaves many interesting research directions open for further investigations. One challenging issue regards the introduction of further nonlinear elements in the system, such as bistable springs, to obtain larger deformations with the same voltage range [33]. The introduction of these components strongly increases the need of nonlinear feedback controllers motivating further research in this direction. Even though this paper has partly considered the problem of robustness with respect to model uncertainties, the study of the reaction of both polymer and electrodes on long-time use (e.g., time-varying damping, creep phenomena) and the ability of feedback control to address these changes is another important research direction. As also pointed out in [44], a further research step which could dramatically influence the penetration of DEAPs in mechatronic industry concerns the development of self-sensing approaches, in which the deformation of the membrane (and therefore the position of the load) is estimated by measures of electrical quantities, such as the capacitance, avoiding the need of position sensors in the control loop. The accurate modeling and compensation of the nonlinearities, as well as the analysis of closed loop performances carried out in this paper are certainly useful steps in the direction of this challenging goal.

VII. ACKNOWLEDGEMENT

The authors wish to thank the anonymous reviewers for their valuable suggestions.

TABLE V
PID CONTROLLERS PERFORMANCE

Controller	$\ e\ _2$ [mm·ms ^{0.5}]	mean(e_{ss}) [μm]	mean($e_{ss,sat}$) [μm]
<i>PID</i> / <i>TD</i> (1.25 kV)	6.87	0.60	0.75
<i>PID</i> / <i>TD</i> (2.5 kV)	9.06	8.85	4.65
<i>NPID</i> / <i>TD</i> (0 kV)	6.89	0.15	1.65
<i>NPID</i> / <i>TD</i> (1.25 kV)	7.07	0.15	1.95
<i>NPID</i> / <i>TD</i> (1.77 kV)	7.24	0.15	2.25
<i>NPID</i> / <i>TD</i> (2.5 kV)	7.67	0.30	3.15
<i>NPID</i> / <i>TDO</i> (1.77 kV)	4.92	0.15	.075
<i>NPID</i> / <i>H_∞D</i> (1.77 kV)	4.65	0.15	0.60

TABLE VI
PID CONTROLLERS PERFORMANCE,
FILTERED REFERENCE

Controller	$\ e\ _2$ [mm·ms ^{0.5}]	$\ e\ _\infty$ [μm]	mean(e_{ss}) [μm]	mean($e_{ss,sat}$) [μm]
<i>PID</i> / <i>TD</i> (1.25 kV)	5.52	410	0.15	0.15
<i>PID</i> / <i>TD</i> (2.5 kV)	8.16	446	10.35	6.60
<i>NPID</i> / <i>TD</i> (0 kV)	5.62	380	0.15	1.95
<i>NPID</i> / <i>TD</i> (1.25 kV)	5.80	386	0.15	1.50
<i>NPID</i> / <i>TD</i> (1.77 kV)	6.05	392	0.15	1.95
<i>NPID</i> / <i>TD</i> (2.5 kV)	6.55	404	0.45	3.75
<i>NPID</i> / <i>TDO</i> (1.77 kV)	3.28	275	0.15	0.90
<i>NPID</i> / <i>H_∞D</i> (1.77 kV)	3.00	260	0.15	0.75

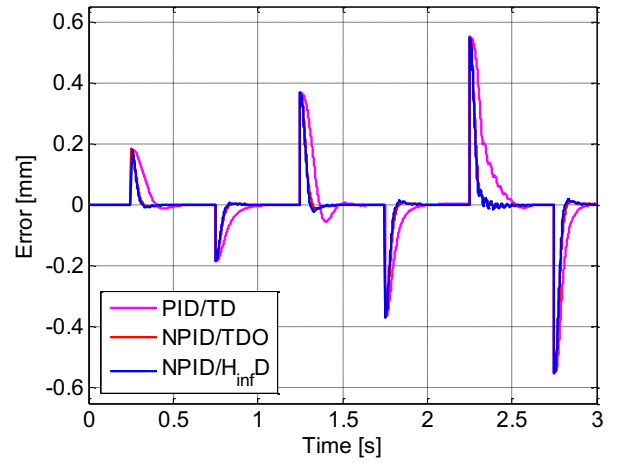


Fig. 18. Tracking error comparison for different controllers, *PID*/*TD*(1.25 kV), *NPID*/*TDO*(1.77 kV) and *NPID*/*H_∞D*(1.77 kV), experimental data.

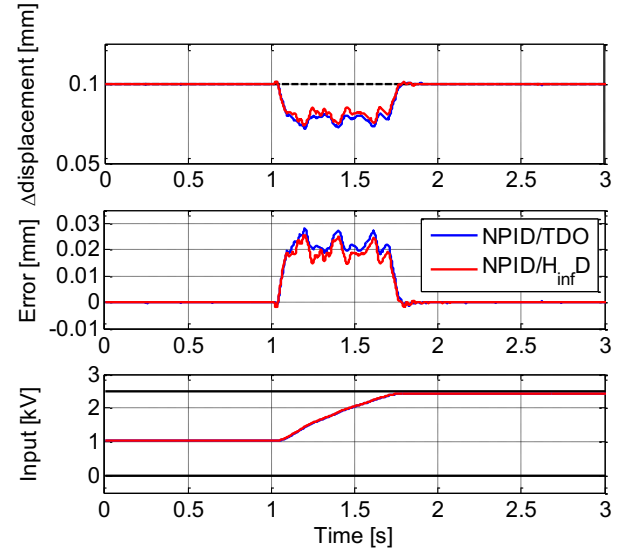


Fig. 19. Disturbance rejection comparison, experimental results, *NPID*/*TDO*(1.77 kV) and *NPID*/*H_∞D*(1.77 kV).

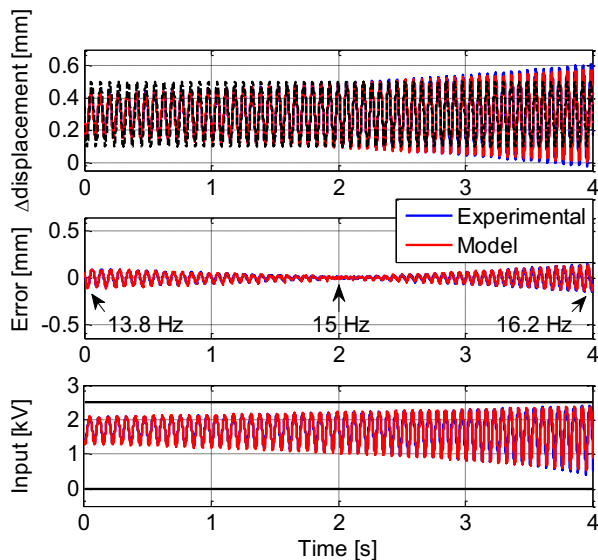


Fig. 20. NPIR, with nonlinearity compensation, Sine sweep input around 15 Hz.

REFERENCES

- [1] N. C. Goulbourne, M. I. Frecker, and E. Mockensturm, "Electro-elastic modeling of a dielectric elastomer diaphragm for a prosthetic blood pump", *Smart Structures and Materials*, 2004, pp. 122–133.
- [2] J. J. Loverich, I. Kanno, and H. Kotera, "Concepts for a new class of all-polymer micropumps" *Lab Chip*, vol. 6, no. 9, pp. 1147–54, Sep. 2006.
- [3] F. Carpi, C. Menon, and D. De Rossi, "Electroactive Elastomeric Actuator for All-Polymer Linear Peristaltic Pumps", *IEEE/ASME Trans. Mechatronics*, vol. 15, no. 3, pp. 460–470, Jun. 2010.
- [4] P. Lotz, M. Matyssek, and H. F. Schlaak, "Fabrication and Application of Miniaturized Dielectric Elastomer Stack Actuators", *IEEE/ASME Trans. Mechatronics*, vol. 16, no. 1, pp. 58–66, Feb. 2011.
- [5] Y.-Y. J. Fu, C.-M. Huang, C.-C. Hsieh, and Chien-Chung, "Improvement of viscoelastic effects of dielectric elastomer actuator and its application for valve devices", *Electroact. Polym. Actuators Devices (EAPAD)*, Y. Bar-Cohen, ed., p. 65241Y–65241Y–9.
- [6] M. Giousouf and G. Kovacs, "Dielectric elastomer actuators used for pneumatic valve technology", *Smart Mater. Struct.*, vol. 22, no. 10, p. 104010, Oct. 2013.
- [7] R. Heydt, R. Kornbluh, J. Eckerle, and R. Pelrine, "Sound radiation properties of dielectric elastomer electroactive polymer loudspeakers", *Smart Structures and Materials 2006: Electroactive Polymer Actuators and Devices (EAPAD)*, Y. Bar-Cohen, ed., p. 61681M–61681M–8.
- [8] T. Sugimoto, A. Ando, K. Ono, Y. Morita, K. Hosoda, D. Ishii, and K. Nakamura, "A lightweight push-pull acoustic transducer composed of a pair of dielectric elastomer films", *J. Acoust. Soc. Am.*, vol. 134, no. 5, pp. EL432–7, Nov. 2013.
- [9] R. Pelrine, R. D. Kornbluh, Q. Pei, S. Stanford, S. Oh, J. Eckerle, R. J. Full, M. a. Rosenthal, and K. Meijer, "Dielectric Elastomer Artificial Muscle Actuators: Toward Biomimetic Motion", *Proc. SPIE 4695, Smart Structures and Materials 2002: Electroactive Polymer Actuators and Devices (EAPAD)*, 126 vol. 4695, pp. 126–137, Jul. 2002.
- [10] A. Wingert, M. D. Lichter, S. Dubowsky, and M. Hafez, "Hyper-Redundant Robot Manipulators Actuated by Optimized Binary Dielectric Polymers", *SPIE* vol. 4695, pp. 415–423, Jul. 2002.
- [11] J.-S. Plante, "Dielectric Elastomer Actuators for Binary Robotics and Mechatronics", *Massachusetts Institute of Technology*, 2006, pp. 1–186.
- [12] H. Kim, J. Park, N. H. Chuc, H. R. Choi, J. D. Nam, Y. Lee, H. S. Jung, and J. C. Koo, "Development of dielectric elastomer driven micro-optical zoom lens system", *Proc. SPIE 6524, Electroact. Polym. Actuators Devices (EAPAD)*, Y. Bar-Cohen, ed., p. 65241V–65241V–10, 2007.
- [13] C. Keplinger, M. Kaltenbrunner, N. Arnold, and S. Bauer, "Röntgen's electrode-free elastomer actuators without electromechanical pull-in instability", *Proc. Natl. Acad. Sci. U. S. A.*, vol. 107, no. 10, pp. 4505–10, Mar. 2010.
- [14] S. Son, D. Pugal, T. Hwang, H. R. Choi, J. C. Koo, Y. Lee, K. Kim, and J.-D. Nam, "Electromechanically driven variable-focus lens based on transparent dielectric elastomer", *Appl. Opt.*, vol. 51, no. 15, pp. 2987–96, May 2012.
- [15] G. Jordan, D. N. McCarthy, N. Schleppe, J. Krißler, H. Schröder, and G. Kofod, "Actuated Micro-optical Submount Using a Dielectric Elastomer Actuator", *IEEE/ASME Transactions on Mechatronics*, vol. 16, no. 1, pp. 98–102, 2011.
- [16] J. Plante and S. Dubowsky, "On the performance mechanisms of Dielectric Elastomer Actuators", *Sensors Actuators A Phys.*, vol. 137, no. 1, pp. 96–109, 2007.
- [17] A. York, J. Dunn, and S. Seelecke, "Experimental characterization of the hysteretic and rate-dependent electromechanical behavior of dielectric electro-active polymer actuators", *Smart Mater. Struct.*, vol. 19, no. 9, p. 094014, Sep. 2010.
- [18] M. Hodgins, A. York, and S. Seelecke, "Modeling and experimental validation of a bi-stable out-of-plane DEAP actuator system", *Smart Mater. Struct.*, vol. 20, no. 9, p. 094012, Sep. 2011.
- [19] G. Kofod, P. Sommer-Larsen, R. Kornbluh, and R. Pelrine, "Actuation Response of Polyacrylate Dielectric Elastomers", *J. Intell. Mater. Syst. Struct.*, vol. 14, no. 12, pp. 787–793, Dec. 2003.
- [20] C. M. Hackl, H. Tang, S. Member, R. D. Lorenz, and L. Turng, "A Multidomain Model of Planar Electro-Active Polymer Actuators", *IEEE transactions on industry applications*, vol. 41, no. 5, pp. 1142–1148, 2005.
- [21] M. Wissler and E. Mazza, "Mechanical behavior of an acrylic elastomer used in dielectric elastomer actuators", *Sensors Actuators A Phys.*, vol. 134, no. 2, pp. 494–504, Mar. 2007.
- [22] W. Kaal and S. Herold, "Electroactive Polymer Actuators in Dynamic Applications", *IEEE ASME Trans. Mechatronics*, vol. 16, no. 1, pp. 24–32, 2011.
- [23] G. Berselli, R. Verthey, M. Babic, and V. Parenti Castelli, "Dynamic modeling and experimental evaluation of a constant-force dielectric elastomer actuator", *J. Intell. Mater. Syst. Struct.*, vol. 24, no. 6, pp. 779–791, Aug. 2012.
- [24] M. Hodgins, G. Rizzello, A. York, and S. Seelecke, "High-Frequency Dynamic Model of a Pre-Loaded Circular Dielectric Electro-Active Polymer Actuator", *Proc. ASME 2013 Conf. Smart Mater. Adapt. Struct. Intell. Syst. SMASIS2013*, pp. 1–10.
- [25] G. Rizzello, D. Naso, A. York, and S. Seelecke, "A Nonlinear Electro-Mechanical Model for an Annular Dielectric Elastomer Actuator with a Biasing Mass", *VDI Mechatronik 2013*, pp. 1–6, Aachen, March, 06–08, 2013.
- [26] G. Moretti, M. M. Fontana, T. Verthey, "Modeling and Control Of Lozenge-Shaped Dielectric Elastomer Generators", *Proc. ASME 2013 Conf. Smart Mater. Adapt. Struct. Intell. Syst. SMASIS2013*, pp. 1–10.
- [27] S. Q. Xie, P. F. Ramson, D. Graaf, E. P. Calius, and I. a. Anderson, "An Adaptive Control System for Dielectric Elastomers", *2005 IEEE Int. Conf. Ind. Technol.*, pp. 335–340, 2005.
- [28] M. Randazzo, M. Fumagalli, G. Metta, and G. Sandini, "Closed loop control of a rotational joint driven by two antagonistic dielectric elastomer actuators", *Proc. SPIE 7642, Electroactive Polymer Actuators and Devices (EAPAD) 2010*, 76422D (April 09, 2010); doi:10.1117/12.847372.
- [29] R. W. Jones and R. Sarban, "Inverse grey-box model-based control of a dielectric elastomer actuator", *Smart Mater. Struct.*, vol. 21, 075019, Jul. 2012.
- [30] R. Sarban and R. W. Jones, "Physical model-based active vibration control using a dielectric elastomer actuator", *J. Intell. Mater. Syst. Struct.*, vol. 23, no. 4, pp. 473–483, Feb. 2012.
- [31] E. D. Wilson, T. Assaf, M. J. Pearson, J. M. Rossiter, S. R. Anderson, and J. Porriall, "Bioinspired Adaptive Control for Artificial Muscles", *Biomimetic and Biohybrid Systems, Lecture Notes in Computer Science Volume 8064*, 2013, pp. 311–322.
- [32] G. Rizzello, D. Naso, A. York, and S. Seelecke, "Modeling and Position Control of an Electromechanical Actuator Based on a Mass-Spring-Biased EAP System," *ETFA2013, 18th IEEE International Conference on Emerging Technologies and Factory Automation*, pp. 1–8, Cagliari, 11–13 Sept. 2013.
- [33] M. Hodgins, A. York, and S. Seelecke, "Experimental comparison of bias elements for out-of-plane DEAP actuator system", *Smart Mater. Struct.* 22 094016. doi:10.1088/0964-1726/22/9/094016.
- [34] J. A. Stratton, *"Electromagnetic Theory"*, McGraw-Hill Book Company, Inc., London, 1941.
- [35] J. Plante and S. Dubowsky, "Large-scale failure modes of dielectric elastomer actuators", *Int. J. Solids Struct.*, vol. 43, no. 25–26, pp. 7727–7751, Dec. 2006.
- [36] Z. Suo, "Theory of dielectric elastomers", *Acta Mech. Solida Sin.*, vol. 23, no. 6, 2010.
- [37] T. He, L. Cui, C. Chen, and Z. Suo, "Nonlinear deformation analysis of a dielectric elastomer membrane-spring system", *Smart Mater. Struct.*, vol. 19, no. 8, p. 085017 (7 pp.), Aug. 2010.

- [38] M. Wissler and E. Mazza, "Modeling of a pre-strained circular actuator made of dielectric elastomers", *Sensors Actuators A Phys.*, vol. 120, no. 1, pp. 184–192, Apr. 2005.
- [39] "*Properties and Behavior of Polymers*", John Wiley & Sons, Inc., Hoboken, New Jersey, 2011.
- [40] J. Jang, C. Sun, and E. Mizutani, "*Neuro-fuzzy and soft computing: a computational approach to learning and machine intelligence*", Prentice-Hall, Englewood Cliffs, New Jersey, 1997.
- [41] K. Åström, R. Murray, "*Feedback systems: an introduction for scientists and engineers*", Princeton University Press, Princeton and Oxford, 2008.
- [42] S. Skogestad and I. Postlethwaite, "Multivariable feedback control: analysis and design", John Wiley & sons, Inc., New York, 2005.
- [43] J. Shamma, "Robust stability with time-varying structured uncertainty", *IEEE Trans. Autom. Control*. Vol. 39, No. 4, 1994.
- [44] York, A., & Seelecke, S.. "Towards Self-Sensing of DEAP Actuators: Capacitive Sensing Experimental Analysis". *ASME 2010 Conference on Smart Materials, Adaptive Structures and Intelligent Systems*, pp. 307-314, American Society of Mechanical Engineers.